



### **Science Arts & Métiers (SAM)**

is an open access repository that collects the work of Arts et Métiers Institute of Technology researchers and makes it freely available over the web where possible.

This is an author-deposited version published in: <https://sam.ensam.eu>  
Handle ID: [.http://hdl.handle.net/10985/10861](http://hdl.handle.net/10985/10861)

#### **To cite this version :**

Samir Chandra ROY, Jean-Pierre FRANC, Nicolas RANC, Marc FIVEL - Determination of cavitation load spectra—Part 2: Dynamic finite element approach - Wear - Vol. 344-345, p.120–129 - 2015

Any correspondence concerning this service should be sent to the repository

Administrator : [scienceouverte@ensam.eu](mailto:scienceouverte@ensam.eu)



# Determination of cavitation load spectra—Part 2: Dynamic finite element approach

Samir Chandra Roy <sup>a,\*</sup>, Jean-Pierre Franc <sup>b</sup>, Nicolas Ranc <sup>c</sup>, Marc Fivel <sup>a</sup>

<sup>a</sup> Science and Engineering of Materials and Processes (SIMaP-GPM2), University Grenoble Alpes/CNRS, F-38000 Grenoble, France

<sup>b</sup> Laboratory of Geophysical and Industrial Flows (LEGI), University Grenoble Alpes/CNRS, F-38000 Grenoble, France

<sup>c</sup> Laboratory Procédés et Ingénierie en Mécanique et Matériaux (PIMM), UMR CNRS 8006, Arts et Metiers ParisTech, 151 Boulevard de l'Hopital, 75013 Paris, France

---

## A B S T R A C T

Cavitation erosion is a well-known problem in fluid machineries which occurs due to repeated hydrodynamic impacts caused by cavitation bubble collapse. Cavitation pitting test is often used for the quantification of flow aggressiveness required for lifetime prediction of hydraulic equipment. Understanding the response of the target material under such hydrodynamic impact is essential for correctly interpreting the results obtained by cavitation pitting test. Moreover the proper knowledge of cavitation pitting mechanism would enable us to design new materials more resistant to cavitation erosion. In this paper, the dynamic behavior of three materials 7075 Aluminum alloy, 2205 duplex stainless steel and Nickel–Aluminum Bronze under cavitation hydrodynamic impact has been studied in details by using finite element simulations. The applied load due to hydrodynamic impact is represented by a Gaussian pressure field which has a peak stress and, space and time evolution of Gaussian type. Mechanism of cavitation pit formation and the effect of inertia and strain rate sensitivity of the materials have been discussed. It is found that if the impact duration is very short compared to a characteristic time of the material based on its natural frequency, no pit would form into the material even if the impact stress is very high. It is also found that strain rate sensitivity reduces the size of the deformed region and thereby could enhance the cavitation erosion resistance of the material.

## 1. Introduction

In hydraulic equipment such as fluid machineries, pipes, ship propellers and valves, cavitation erosion may occur due to repeated hydrodynamic impacts caused by the individual or collective collapse of cavitation bubbles. Initially the material undergoes plastic deformation in the form of cavitation pits and repeated impacts cause strain accumulation leading to damage and material-loss [1,2].

The basic mechanism [1–4] of cavitation erosion is the following. In a high velocity flow, vapor cavities generate usually from trapped micron gas particles in the region where the local pressure drops below the vapor pressure of the fluid. Subsequently, these vapor bubbles collapse in higher pressure regions with the formation of high intensity micro-jets and shock waves. The intensity of such micro-jet and shock wave depends on various parameters including

the pressure gradient, bubble size and distance of bubble collapse from the solid wall.

When the magnitude of such impact load due to the combined or solo effect of micro-jet and shock wave exceeds certain value for which equivalent stress into the target material exceeds the yield strength, a cavitation pit is formed. Repetition of such impacts, which occur randomly in space and time, causes hardening of the surface layer of the target material through plastic deformation [5] and subsequently strain accumulates. When the strain exceeds the ultimate strain, the material starts to degrade locally i.e. damage initiates and continues to propagate until complete failure in terms of material removal occurs.

From an experimental viewpoint, two types of erosion tests are generally done, cavitation pitting test and cavitation erosion test. The main difference between the two is the test duration. Pitting test (introduced by Knapp [6,7]) is done for a short period of time to avoid any mass loss and the pits are considered as the signature of individual bubble collapse. Cavitation pitting test is focused on the assessment of cavitation flow aggressiveness. Erosion test is done for a long period of time to track the mass loss over time, which occurs due to repeated impacts.

---

\* Corresponding author.

E-mail addresses: roysam.nita@gmail.com, samir-chandra.roy@simap.grenoble-inp.fr (S.C. Roy).

Cavitation erosion tests are done to classify materials according to their resistance to cavitation erosion and, as far as possible, to correlate their resistance with material properties like hardness, yield strength, ultimate strength etc. [4]. Various laboratory devices have been developed to carry out accelerated cavitation erosion test such as ultrasonic horns [8,9], cavitating liquid jets [8–12], rotating disks [13] and cavitation tunnels [14,15]. Generally, the rate of mass loss or the erosion depth is used as a measure of cavitation erosion damage. Though these tests are practically used, they are far from being universal and transposition from model to prototype still remains an issue [4]. Recently focuses are being made to an alternative numerical approach to predict mass loss and Fivel et al. [16] have laid down the foundation for such numerical approach.

Regarding the assessment of cavitation flow aggressiveness, conventional or special transducers can be used to measure the impact forces [4,17], which are then converted to impact stresses based on the transducer's exposed surface area. The flow aggressiveness is defined by the frequencies of peak impact stresses as a function of amplitude. Generally the estimated values of peak stresses are not very reliable, because of the transducer's bigger size and higher rise time compared to that of hydrodynamic impact.

To overcome this difficulty, a combined experimental and numerical approach has been developed by Roy et al. [18–20] to estimate the impact stresses as well as their radial extent. The method consists in using an inverse finite element (FE) computation to derive the characteristics of the impact load responsible for each pit identified on a pitted test sample. This enables the better quantification of flow aggressiveness in terms of frequencies of impacts of a given peak stress and radial extent. The approach proposed in [18–20] is however based on static computations. One of the objectives of the present work is to extend it to the dynamic case where density and strain rate sensitivity of the material would play a vital role into the deformation mechanism. The current paper explains in details the feasibility of such method to implement when the complete dynamics of the material deformation is considered. Recently, Pöhl et al. [21] have presented a similar method to estimate impact loads from cavitation pit geometries. Their method is [21] based on static finite element analysis where the material properties were characterized by nanoindentation tests and, the representative pressure field was defined by a bell-shape profile. Two different approaches are presented in references [21,18] to accomplish the same goal of estimating cavitation impact loads.

Each hydrodynamic impact has a characteristic size, peak stress and duration which are related to hydrodynamic parameters. Influence of these three parameters on the dynamics of cavitation pit formation is investigated in this paper. The paper focuses on the influence of impact duration on the mechanism of cavitation erosion that has been less studied in the literature, particularly when the material behavior is strain rate sensitive. Section 2 is devoted to the presentation of material properties with special emphasis on the integration of strain rate sensitivity via the Johnson–Cook model. The numerical model based on the use of the commercial finite element method (FEM) code ABAQUS is presented in Section 3. Section 4 is devoted to presentation of results. It includes a discussion of the effect of impact duration on pit formation, an extension of the inverse FE method presented in [18] to the dynamic case and an evaluation of strain rate during cavitation pit formation. Discussion (Section 5) is largely based on the introduction of a material characteristic time evaluated on the basis of the characteristic size of the plastically deformed volume and the associated natural frequency of the material.

## 2. Material properties

### 2.1. Constitutive model

Three materials 7075 Aluminum alloy (Al-7075), 2205 duplex stainless steel (A-2205) and Nickel–Aluminum Bronze (NAB) have been considered for the current study. Density ( $\rho$ ), Young modulus ( $E$ ) and Poisson ratio ( $\nu$ ) of these materials are presented in Table 1. Material properties were characterized by the Johnson–Cook (JC) plasticity model in the form given by Eq. (1), avoiding the thermal softening part (see [22] for more details about JC plasticity model).

$$\bar{\sigma} = \left( \sigma_y + K \varepsilon_p^n \right) \left( 1 + C \ln \frac{\dot{\varepsilon}_p}{\dot{\varepsilon}_0} \right) \quad (1)$$

Here,  $\varepsilon_p$  is the equivalent plastic strain,  $\dot{\varepsilon}_p$  is the equivalent plastic strain rate and  $\dot{\varepsilon}_0$  is the reference strain rate at which the yield strength  $\sigma_y$ , strength coefficient  $K$  and strain hardening exponent  $n$  should be estimated. Parameter  $C$  is the strain rate sensitivity. At reference strain rate (taken as  $0.05 \text{ s}^{-1}$ )  $\ln(\dot{\varepsilon}_p/\dot{\varepsilon}_0) = 0$ , Eq. (1) becomes a simple Ramberg–Osgood type equation where hardening is a function of  $\varepsilon_p$  only.

### 2.2. Nanoindentation test

Nanoindentation tests were done on these three materials at a strain rate of  $0.05 \text{ s}^{-1}$  using a spherical diamond (Young's modulus,  $E_i = 1141 \text{ GPa}$  and Poisson's ratio,  $\nu_i = 0.07$ ) indenter of radius,  $R = 9.46 \text{ }\mu\text{m}$ . Standard sample preparation procedure- initially polished by using sandpapers reducing grit size till  $8.4 \text{ }\mu\text{m}$  (grade P2500), then polished by using diamond paste gradually reducing the size from  $6$  to  $1 \text{ }\mu\text{m}$  and finally by using colloidal silica of  $0.03 \text{ }\mu\text{m}$  size.

Characterization of material properties by nanoindentation is considered to be relevant to cavitation pitting [20,23], as in both the cases deformation is compressive and confined. Material properties ( $\sigma_y$ ,  $K$  and  $n$ ) were obtained by inverse FEM simulation of nanoindentation, where  $\sigma_y$ ,  $K$  and  $n$  were optimized in order to get a simulated load–displacement curve similar to the experimental one, as explained in details in [20]. Estimated material properties are given in Table 1 and Fig. 1 shows an example of comparison of simulated and experimental load–displacement curves for A-2205.

### 2.3. Integration of strain rate sensitivity

Strain rate involved in cavitation pitting is expected to be very high, up to the order of  $\sim 10^6 \text{ s}^{-1}$  [4,20], and could vary depending on the bubble size and collapse driving pressure gradient. To take into account such strain rate dependencies of cavitation pit formation, compression tests complemented by Split Hopkinson Pressure Bar (SHPB) tests were done on the three materials at strain rates ranging from  $0.001$  to  $\sim 2000 \text{ s}^{-1}$ . Cylindrical specimens of equal length and diameter of  $8 \text{ mm}$  have been used.

Strain rate sensitivity parameter  $C$  was estimated by fitting the Eq. (2) to the experimental data as show in Fig. 2, as an example in

**Table 1**  
Physical and nanoindentation mechanical properties of the materials at strain rate  $0.05 \text{ s}^{-1}$ .

Material	$\rho$ (kg/m <sup>3</sup> )	$E$ [GPa]	$\nu$	$\sigma_y$ [MPa]	$K$ [MPa]	$n$
Al-7075	2810	71.9	0.33	335	396	0.30
A-2205	7805	186	0.30	508	832	0.51
NAB	7580	122	0.32	300	1150	0.58

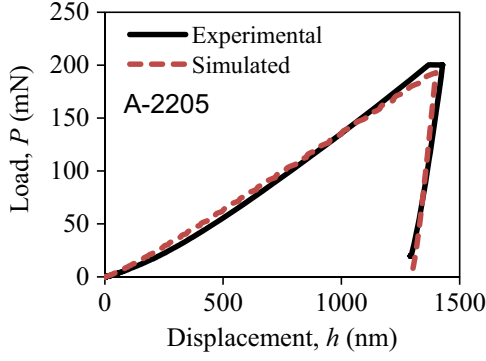


Fig. 1. Comparison of experimental and simulated nanoindentation load-displacement curves of A-2205.

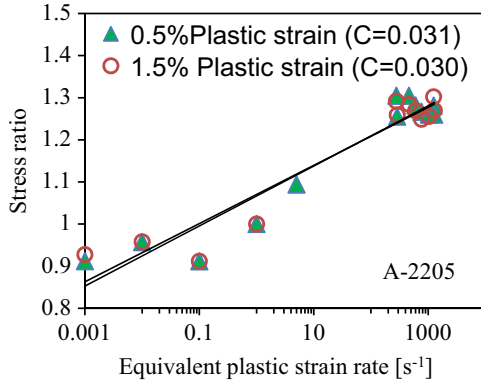


Fig. 2. Stress ratio versus strain rate on a semi-log plot shows almost linear behavior for A-2205. Strain rate sensitivity  $C$  is estimated at 0.5% and 1.5% of plastic strains are almost same.

the case of A-2205. To avoid thermal softening,  $C$  was estimated at lower amount of plastic strain ( $\epsilon_p < 2\%$ ), as can be seen in Fig. 2. The values of  $C$  at 0.5% and 1.5% of plastic strains are almost same.

$$R = \frac{\bar{\sigma}}{\sigma_y + K\epsilon_p^n} = 1 + C \ln \frac{\dot{\epsilon}_p}{\dot{\epsilon}_0} \quad (2)$$

In Eq. (2),  $R$  represents the stress ratio at strain rate  $\dot{\epsilon}_p$  with respect to  $\dot{\epsilon}_0$ . Values of  $C$  were estimated to be 0.0068, 0.031 and 0.0119 for Al-7075, A-2205 and NAB respectively. A-2205 has the maximum strain rate sensitivity whereas the Al-7075 has the minimum strain rate sensitivity.

This way of integration of strain rate sensitivity obtained by compression test with nanoindentation properties to simulate the cavitation pitting behavior is studied in details by Roy et al. [19,20] and found to be appropriate, as the current state of art of nanoindentation testing does not allow test at very high strain rate to estimate strain rate sensitivity properly.

### 3. Simulation and mesh details

The pressure induced by cavitation bubble collapse depends on the standoff distance from the solid wall and has a complex shape in both space and time. Except for the smaller standoff distances when double pressure pulse is expected for each bubble collapse, the pressure field can be described reasonably well by a doubly Gaussian profile [1] as given by Eq. (3), which is supported by

experimental recordings of pressure pulses [17,24].

$$\sigma = \sigma_H \exp \left[ - \left( \frac{2r}{d_H} \right)^2 \right] \exp \left[ - \left( \frac{t - t_{max}}{t_H} \right)^2 \right] \quad (3)$$

In Eq. (3), variables  $t$  and  $r$  represent time and radial extent respectively,  $t_{max}$  is the time when  $\sigma = \sigma_H$  and  $t_H$  is the characteristic impact rise duration in a similar sense to characteristic impact radius  $d_H$  represents characteristic impact diameter).

Dynamic explicit simulations were done in the commercial FEM code ABAQUS using a 2D axisymmetric model (as shown in Fig. 3). ABAQUS dynamic explicit solves structural momentum equation based on a lumped mass matrix corresponding to the mesh. Dynamic explicit solver is preferred for simulation of high rate deformation processes where structural dynamics or stress wave propagation is important. CAX4R (continuum axisymmetric 4 nodes reduced integration) elements were used for the meshing. Model domain size is kept significantly bigger than the impact size (parametrically  $150 \times r_H$ ), to avoid any stress wave reflection from the boundary, so that the domain could be considered infinite compared to that of impacted area. Symmetric boundary condition (XSYMM in ABAQUS) has been used on the axis of symmetry (OA) and displacement along  $z$  direction was restricted at the bottom most side (AC). Plastic behavior of the material was characterized by the Johnson-Cook plasticity model of the form given by Eq. (1).

In order to investigate the dynamics of cavitation pitting, FEM simulations were done with the representative Gaussian pressure field given by Eq. (3) for different values of  $\sigma_H$ ,  $d_H$  and  $t_H$  and, by using the material properties estimated in Section 2.

## 4. Results

### 4.1. Preliminary results

As dynamic explicit solver does not impose any iterative procedure to converge to the solution, the time increment size should be very small for accurate dynamic response of the material. The automatic time incrementation scheme available in ABAQUS is used to avoid any such error, which essentially estimate the increment size which is always less than or equal to the time

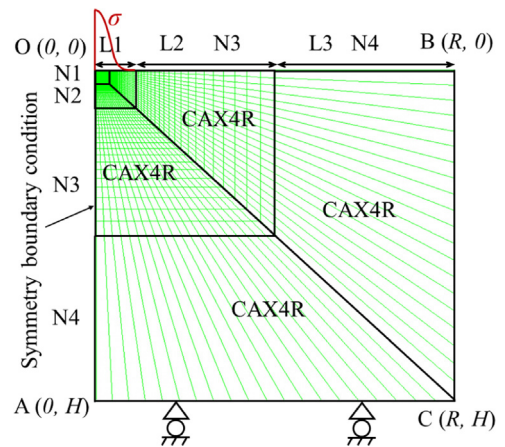
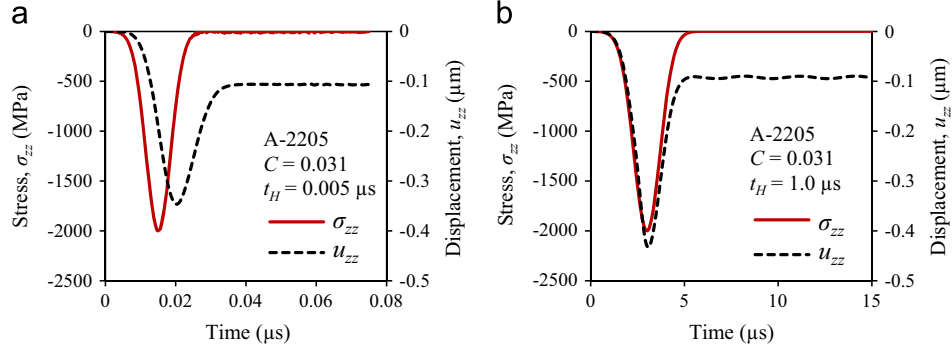


Fig. 3. 2-D axisymmetric mesh used for the numerical simulations. Distances along radial and thickness directions are represented by  $r$  and  $z$  respectively.  $L$  represents length of one or more section as shown by the arrows.  $N$  represents number of elements on the surface of different section.  $R$  and  $H$  represent the maximum radial and vertical sizes of the simulated volume. Number of elements ( $N1$ ,  $N2$ ,  $N3$  and  $N4$ ) in different section is always constant, but section lengths ( $L1$ ,  $L2$  and  $L3$ ) are parameterized from the radius of hydrodynamic pressure field,  $r_H$ , e.g. if  $d_H = 20 \mu\text{m}$ ,  $N1=20$ ,  $N2=60$ ,  $N3=40$  and  $N4=1$  then,  $L1=0.75 \times d_H=15 \mu\text{m}$ ,  $L1+L2=L3=R/2=50 \times L1=750 \mu\text{m}$ ,  $H=R=1500 \mu\text{m}$ , using geometric progression with common ratio of 1.01.



**Fig. 4.** Represents evolution of applied stress ( $\sigma_{zz}$ ) and deformation depth ( $u_{zz}$ ) with time during hydrodynamic impact. Material: A-2205,  $\sigma_H = 2$  GPa and  $d_H = 40$   $\mu\text{m}$  (a)  $t_H = 0.005$   $\mu\text{s}$  (b)  $t_H = 1.0$   $\mu\text{s}$ .

required by sound wave to propagate through the smallest element in the mesh. The accuracy of the materials dynamic response in cavitation pitting was found to be unaffected by the size of the time increment. The influences of number of elements and domain size have also been verified to get an error proof response.

Influence of impact fall duration onto the pit dimensions has been analyzed in details. As an example in the case of A-2205, Fig. 4(a) and (b) shows the evolution of normal stress ( $\sigma_{zz}$ ) and displacement ( $u_{zz}$ ) at the top most point on the axis of symmetry for  $t_H = 0.005$  and  $1.0$   $\mu\text{s}$  respectively, when  $\sigma_H = 2$  GPa and  $d_H = 40$   $\mu\text{m}$ . As can be seen in Fig. 4(a) for hugely dynamic impact, the material was still deforming during the unloading period of the impact, probably because of the inertial effect, and the displacement ( $u_{zz}$ ) reaches the maximum and then elastic recovery takes place and continues even when the applied stress reaches its plateau region. Whereas for  $t_H = 1.0$   $\mu\text{s}$  (Fig. 4(b)), the displacement reaches the maximum almost at the same time when the applied stress ( $\sigma_{zz}$ ) reaches its peak, and then the elastic recovery also takes place and finishes before the applied stress reaches its plateau region. Therefore to get an error free measure of the simulated pit dimensions, sufficient unloading time should be given to the structure to get stabilized, otherwise we could trap the deformation into an intermediate state. In all the cases presented in this paper impact fall duration of  $12 \times t_H$  is applied and found to provide a stabilized structural response.

#### 4.2. Effect of impact duration on cavitation pitting

To investigate the effect of impact duration onto the mechanism of pit formation, a large number of simulations were conducted with characteristic impact rise duration  $t_H$  ranging from  $1 \times 10^{-4}$ – $5 \times 10^5$   $\mu\text{s}$ , which essentially covers the whole range of possible bubble collapse or hydrodynamic impact durations. Impact duration can be considered as  $2 \times t_H$  which includes both the impact rise and fall duration. Moreover, to isolate the effect of inertia from strain rate sensitivity, simulations were done with the JC plasticity model (Eq. (1)) considering  $C=0$  for all the three materials. These two types of simulation results were then compared with static response (in absence of time dependent part of Eq. (3)) of the material under the same loading condition of  $\sigma_H$  and  $d_H$ , where both the inertial and strain rate sensitive effects are absent. As an example in the case of A-2205, Fig. 5 shows the variation of pit depth ( $h_p$ ) with  $t_H$  for a constant value of  $\sigma_H = 3$  GPa and  $d_H = 40$   $\mu\text{m}$ . As can be seen, with increase in  $t_H$  both the dynamic solutions, with ( $C=0.031$ ) and without ( $C=0$ ) the strain rate sensitivity effect, the dynamic solution converges towards the static solution and in both the cases a peak has been observed.

In both the dynamic cases, with or without strain rate sensitivity, pit depth initially increases with increase in  $t_H$ , reaches a

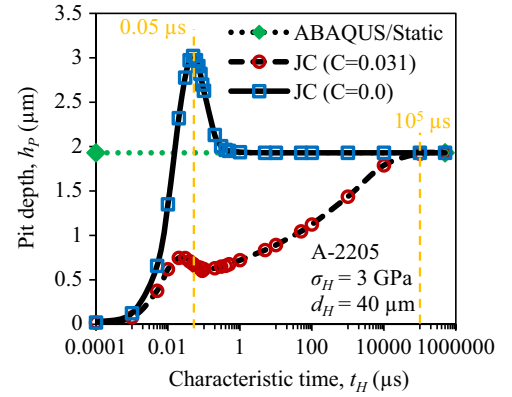


**Fig. 5.** Variation of pit depths ( $h_p$ ) with characteristic impact rise duration  $t_H$  (log-scale). Material: A-2205,  $\sigma_H = 3$  GPa,  $d_H = 40$   $\mu\text{m}$  and  $t_H$  ranges from  $1 \times 10^{-4}$  to  $5 \times 10^5$   $\mu\text{s}$ . Static solutions is time independent and the virtual dotted line highlights the same. (For interpretation of the references to color in this figure, the reader is referred to the web version of this article.)

peak, then again decreases and thereafter for strain rate insensitive behavior the pit depth remains unchanged, whereas for strain rate sensitive behavior pit depth continues to increase again, until the hardening due to strain rate sensitivity is diminished. With the inclusion of strain rate sensitivity, the characteristic time  $t_H$  at which the peak is observed decreased from  $0.05$  to  $0.02$   $\mu\text{s}$ . This could be due to the natural frequency of the material, which increases with increase in stiffness and there by reduces the characteristic time or natural period of the material.

One important phenomenon to be noticed, after  $t_H \geq 0.5$   $\mu\text{s}$ , the dynamic solution with  $C=0$  is identical i.e. the inertial effect becomes insignificant with respect to the pit dimension. Similar behavior was also observed in Al-7075 and NAB with the occurrence of peak at values of  $t_H$  close to  $0.05$   $\mu\text{s}$  (orange dashed line in Fig. 5). Thus in the case of real cavitation hydrodynamic impact, if the impact duration is in the order of microsecond, we can possibly avoid the dynamic effect due to inertia for the inverse calculation of  $\sigma_H$  and  $d_H$  from cavitation pit geometry, as done by Roy et al. [18–20]. However, it should be emphasized that time dependent strain rate sensitivity of the material should be considered for accurate estimations using such inverse method. Although it is difficult to accurately measure the impact duration by using pressure transducer, some observations suggest that impact duration generally varies in the order of microsecond [1,17,24].

In the presence of positive strain rate sensitivity, as shown in Fig. 5 (by JC ( $C=0.031$ )), the material becomes harder and the pit depth gets reduced, especially in the time domain where the strain rate sensitivity is effective in the deformation mechanism. For

characteristic impact rise duration  $t_H > 10^5 \mu\text{s}$  (orange dashed line in Fig. 5), the strain rate sensitivity is also found to disappear from the deformation behavior. As  $10^5 \mu\text{s}$  is a quite large value for impact rise duration, it can be considered that for metal subjected to cavitation erosion, strain rate sensitivity would always play a key role in the erosion mechanism. As the strain rate sensitivity reduces the pit depth, it can be assumed that, in case of high strain rate sensitive material (like A-2205), less volume of the material will be affected by a similar hydrodynamic impact compared to that of a less strain rate sensitive material (like Al-7075). For example, Al-7075 and NAB have almost the same level of yield strength, but the strain rate sensitivity of NAB is 1.75 times more than Al-7075, and it was experimentally observed that cavitation erosion damage in Al-7075 is significantly higher than NAB [25]. For A-2205, the minimum erosion rate was observed as both the yield strength and strain rate sensitivity for A-2205 is the highest among the three materials. Thus we could say if a material has higher yield strength as well as higher strain rate sensitivity, the erosion resistance of that material would be greater.

One more important observation can be drawn from Fig. 5, as  $t_H$  approaches to zero, the pit depth also approaches to zero in both the cases of dynamic simulations. As an example, for  $t_H = 10^{-4} \mu\text{s}$ , the pit depth  $h_p$  is estimated to be  $\sim 0.01 \mu\text{m}$ . This indicates that even if the impact pressure is high (here  $\sigma_H = 3 \text{ GPa}$ ), the hugely dynamic impacts for which the impact duration is in the order of less than a nanosecond, might not be able to produce any detectable pit. This phenomenon imposes a limitation to the target material, if used as a pressure sensor in cavitation pitting like authors did in [19,20], the material will not reveal impacts of very small duration. Reason of such behavior could be related to the natural frequency of the materials and is discussed in details in Section 5. It can also be assumed that, when the impact duration is very short, the rate of deformation is very high and hence most of the impact energy is transformed into kinetic energy, less energy remains available for work-done in terms of material deformation.

Fig. 6 shows the effect of  $t_H$  on the pit shape for constant values of  $\sigma_H = 3 \text{ GPa}$  and  $d_H = 40 \mu\text{m}$ . Pit shapes have been plotted for some selected values of  $t_H$  to highlight the evolution pattern. Fig. 6(a) shows the variation of pit shapes in absence of strain rate sensitivity, whereas Fig. 6(b) shows the same in presence of strain rate sensitivity. In both the cases, pit shape, especially the depth, changes with  $t_H$  and ultimately attains the pit shape obtained by static simulation, after  $0.5 \mu\text{s}$  in the case  $C=0$  and after  $10^5 \mu\text{s}$  in the case  $C=0.031$ . As can be seen in Fig. 6(a), for  $t_H = 0.05 \mu\text{s}$  pit volume is maximum and it decreases with both increase or decrease in  $t_H$ . Thus it can be considered that for such impacts, when a material has minor strain rate sensitivity,

cavitation erosion damage could also be enhanced by the increased volume of deformation, whereas strain rate sensitivity would always reduce the volume of deformation, as can be seen in Fig. 6(b).

#### 4.3. Effect of $\sigma_H$ and $d_H$ on the dynamics of cavitation pitting

Here the analyses are focused on the dynamic behavior of the material with the highest strain rate sensitivity: A-2205. To analyze the effect of  $d_H$ , simulations were done with different values of  $d_H$  (10, 20, 40, 80 and  $160 \mu\text{m}$ ) keeping a constant value of  $\sigma_H = 3 \text{ GPa}$ , while in each case  $t_H$  was varied from 0.001 to  $1 \mu\text{s}$ . This range of  $t_H$  is chosen as the dynamic behavior is crucial in this time domain, as can be seen in Fig. 5. Pit depth,  $h_p$  versus characteristic time  $t_H$  has been plotted on a log-log graph as shown in Fig. 7 for all the simulations. The values of  $t_H$  at which the peak in pit depth  $h_p$  occurs, increases with  $d_H$  as shown by the arrow connecting the peaks and Section 5 explains a probable reason for this.

To analyze the effect of  $\sigma_H$ , simulations were done with different values of  $\sigma_H$  (2, 3, 4, 5 and  $6 \text{ GPa}$ ) keeping a constant value of  $d_H = 40 \mu\text{m}$ , while in each case  $t_H$  was varied from 0.001 to  $1 \mu\text{s}$ . The values of  $t_H$  at which the peak in pit depth  $h_p$  occurs, increases with  $\sigma_H$  as shown by the arrow connecting the peaks in Fig. 8.

Based on the observations from Figs. 7 and 8, it can be concluded that all the three parameters  $\sigma_H$ ,  $d_H$  and  $t_H$  of hydrodynamic impact influence the dynamics of cavitation pitting, and thereby cavitation erosion. Pit depth increases with increase in both  $\sigma_H$  and  $d_H$ , whereas with  $t_H$  the variation is complex.

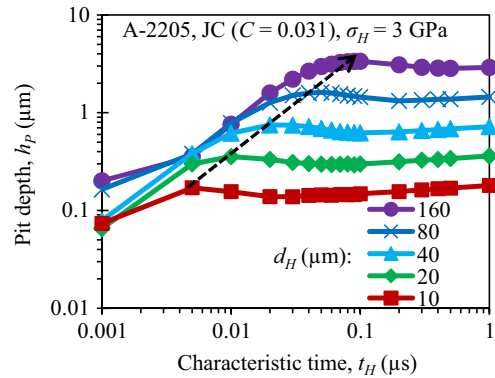


Fig. 7. Variation of pit depth,  $h_p$  with characteristic impact rise duration  $t_H$  with  $\sigma_H = 3 \text{ GPa}$  and  $d_H = 10, 20, 40, 80$  and  $160 \mu\text{m}$ . The data for A-2205 is plotted on log-log scale.

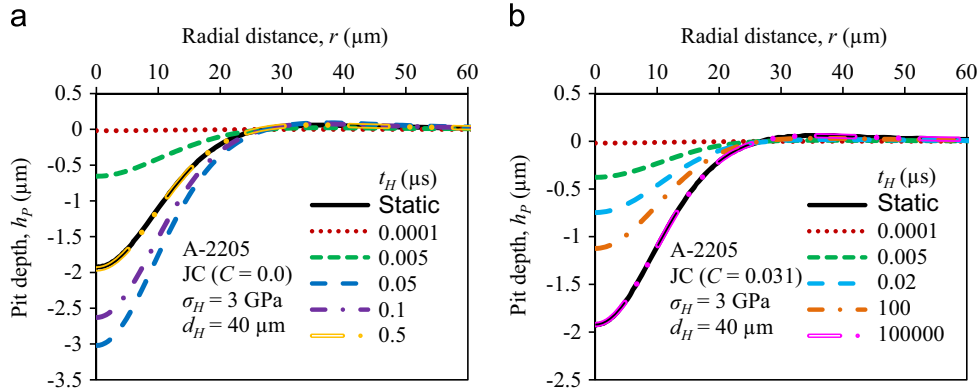


Fig. 6. Variation of pit shape with characteristic impact rise duration  $t_H$  shown for A-2205,  $\sigma_H = 3 \text{ GPa}$  and  $d_H = 40 \mu\text{m}$ . (a) in case of strain rate insensitive behavior ( $C=0$ ) and (b) in case of strain rate sensitive behavior ( $C=0.031$ ). Static Shape represents the pit shape obtained by ABAQUS static analysis with the same values of  $\sigma_H$  and  $d_H$ . (For interpretation of the references to color in this figure, the reader is referred to the web version of this article.)

## 5. Discussion

### 5.1. Mechanism of cavitation pitting

In cavitation pitting the target material size is infinite compared to the size of the hydrodynamic impact and it is difficult to know the real volume of the material which is affected by the impact. One option would be the numerical analysis of the stress or strain field into the material using certain criterion, for example yield stress or 0.2% plastic strain. Fig. 9 shows the schematic of the applied Gaussian pressure load and, the strain field in A-2205 material while impacted with  $\sigma_H = 3$  GPa and  $d_H = 40$   $\mu\text{m}$  for a rise duration of  $t_H = 0.02$   $\mu\text{s}$ . As can be seen, maximum strain occurs inside the material on the axis of symmetry and the plastic domain is confined into a small region. The plastically deformed volume of the material could be confined into a cylinder of radius,  $r_d$  and length,  $l_d$  as shown in Fig. 9. The values of  $r_d$  and  $l_d$  will depend on the values of  $\sigma_H$ ,  $d_H$  and  $t_H$  of the impact load and also on the material constitutive laws.

The dependencies of the plastic strain field size (strain  $> 0.2\%$ ) on  $\sigma_H$  and  $d_H$  has been analyzed. When  $\sigma_H$  and  $t_H$  both are constant, the ratio of  $l_d/d_H$  remains almost constant for any value of  $d_H$ . Whereas, when  $d_H$  and  $t_H$  both are constant, as shown in Fig. 10 (a log-log plot), the ratio of  $l_d/d_H$  varies with  $\sigma_H$  which can be expressed by a power law equation as shown in Eq. (4).

$$l_d/d_H = S_1 \sigma_H^{S_2} \quad (4)$$

In Eq. (4),  $S_1$  and  $S_2$  are two fitting parameters which depend on the material properties. As shown in Fig. 10, when  $t_H \geq 0.01$   $\mu\text{s}$

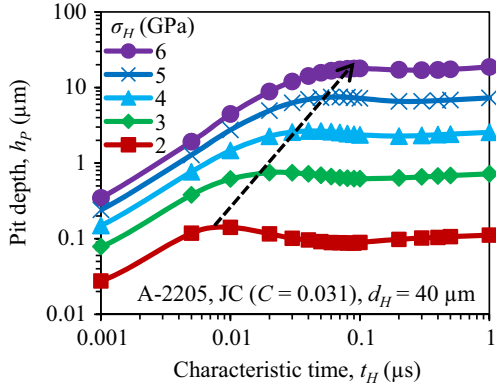


Fig. 8. Variation of pit depth,  $h_p$  with characteristic impact rise duration  $t_H$  with  $\sigma_H = 2, 3, 4, 5$  and  $6$  GPa and  $d_H = 40$   $\mu\text{m}$ . The data for A-2205 is plotted on log-log scale.

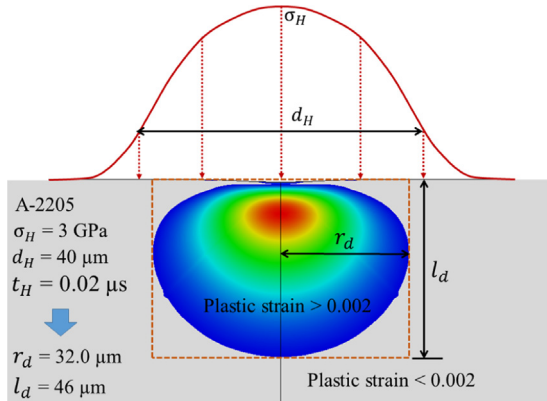


Fig. 9. Schematic of the applied Gaussian pressure field and the strain field in A-2205 material, impacted with  $\sigma_H = 3$  GPa and  $d_H = 40$   $\mu\text{m}$  for a period of  $t_H = 0.02$   $\mu\text{s}$ . plastic strain  $> 0.2\%$  is used for determining the domain size.

the plots of  $l_d/d_H$  versus  $\sigma_H$  are almost identical which can be represented by a single curve (dashed line). Therefore, for the sake of simplicity, time dependencies of  $S_1$  and  $S_2$  is not considered here and the values are estimated to be  $S_1 = 0.0002$  and  $S_2 = 1.0563$ , as shown in Fig. 10. The benefit of using a power law is, when  $\sigma_H = 0$  or  $d_H = 0$ , the value of  $l_d = 0$ .

Using the estimated values of  $S_1$  and  $S_2$ , we can estimate the approximate values of  $l_d$  corresponding to each data in Figs. 7 and 8. These estimated values will be used to adimensionalize the plots in Figs. 7 and 8 in the following section.

The objective here is to find out if the peaks observed in Figs. 5, 7 and 8 are related to the natural frequency of the material or not, as it is well know that, when the applied load frequency is close to the natural frequency of the material then the maximum deflection occurs.

For a spring mass damper system under external load of sinusoidal form, the amplitude of oscillation of the steady state response could be written by the following Eq. (5) (for more details see [26]).

$$X = \frac{F}{k} \frac{1}{\sqrt{(1-\theta^2)^2 + 4\xi^2\theta^2}} \quad (5)$$

In Eq. (5),  $F$  is the amplitude of the external force,  $k$  is the stiffness of the spring,  $\theta = \omega/\omega_n$  (i.e. ratio of angular frequency of the applied load  $\omega$  to the angular natural frequency  $\omega_n$  where  $\omega_n = \sqrt{k/m} = 2\pi f_n$  ( $f_n$  represents the natural frequency in Hz)),  $\xi = b/(2\sqrt{km})$  is the damping ratio where  $b$  is the damping coefficient and  $m$  is the mass.

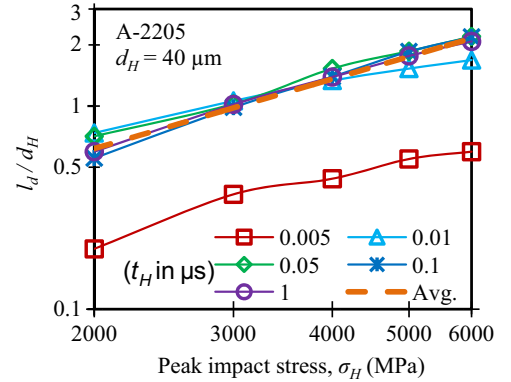


Fig. 10. Variation of normalized plastic strain domain size ( $l_d/d_H$ ) with peak impact stress ( $\sigma_H$ ) is plotted on a log-log scale. Material: A-2205,  $d_H = 40$   $\mu\text{m}$  and  $t_H = 0.005-1$   $\mu\text{s}$ .

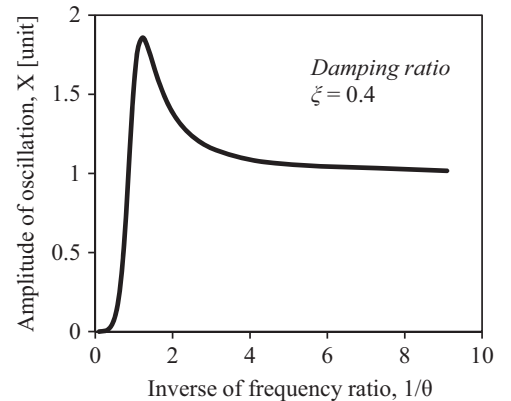


Fig. 11. Amplitude of oscillation  $X$  as a function of inverse of frequency ratio  $1/\theta$  of a spring mass damper system under external force of sinusoidal form, plotted using Eq. (5).

The analytical plot of the amplitude of oscillation  $X$  as a function of  $1/\theta$  using Eq. (5) and assuming constants  $F/k=1$  and  $\xi=0.4$  is shown in Fig. 11. Assumptions of  $F/k=1$  is arbitrary as it is insignificant in the current context, and  $\xi=0.4$  is also arbitrary but represents an under-damped system ( $\xi < 1$ ).

In cavitation pitting, the presence of plasticity would change the stiffness and damping coefficient of the impact affected region of the material with time, leading to potential changes in natural frequency. The dynamic response of the spring mass damper system as shown in Fig. 11 however interestingly resembles very well the dynamic behavior of the material under cavitation pitting as shown in Figs. 5, 7 and 8. As stated, it can be noticed in Fig. 5 that the strain rate sensitivity changes the dynamic behavior significantly, however, the basic behavior remains the same with the occurrence of a peak.

Now by comparing the dynamics of cavitation pitting with that of spring mass damper system we shall try to find out some kind of natural frequency for the material under cavitation impact. It should be emphasized here that Eq. (5) is mainly derived from the equation of motion for elastic response of spring or wire system. The purpose here is to qualitatively understand the mechanism of cavitation pitting rather than estimating something very precise.

An approximate estimation of the natural frequency of the material under cavitation impact can be done based on the representative cylindrical volume of radius,  $r_d$  and length,  $l_d$  as shown in Fig. 9 and can be written as given by Eq. (6).

$$f_n = \frac{1}{2\pi} \sqrt{\frac{k}{m}} = \frac{1}{2\pi l_d} \sqrt{\frac{E}{\rho}} \quad (6)$$

In Eq. (6),  $E$  is Young's modulus,  $\rho$  is the density of the material and for the representative cylinder (in Fig. 9)  $k = \pi r_d^2 E / l_d$  and  $m = \pi r_d^2 l_d \rho$ .

From Eq. (6), the natural period of the material  $t_{mat}$  in cavitation pitting can be estimated as  $t_{mat} = 1/f_n$ . Using Eq. (4), the values of  $l_d$  have been estimated for all the data in Figs. 7 and 8, and corresponding  $t_{mat}$  have also been estimated by using the estimated values of  $l_d$  in Eq. (6). Figs. 7 and 8 have been re-plotted by normalizing  $h_p$  with  $l_d$  and  $t_H$  with  $t_{mat}$  as shown in Figs. 12 and 13 respectively. Unlike before,  $2 \times t_H$  is considered instead of  $t_H$ , as it could be considered as impact duration which includes both the rise and fall duration of the hydrodynamic impact.

As can be seen in Fig. 12, all the peaks for different values of  $d_H$  at constant value of  $\sigma_H$  are now aligned at the same point ( $2 \times t_H / t_{mat} \approx 1$ , as shown by the dotted line) on the horizontal axis. This indicates that the peaks are indeed related to the frequency of the impact load, which is close to the natural frequency

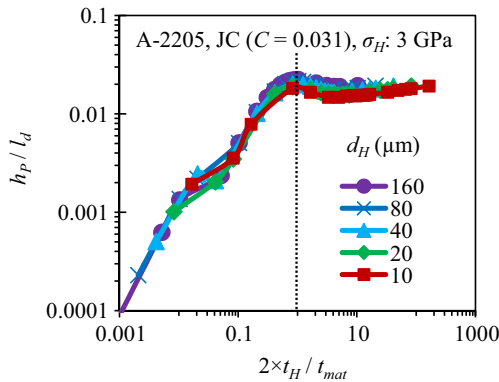


Fig. 12. Variation of pit depth  $h_p$  normalized by plastic strain field size  $l_d$  versus impact duration  $2 \times t_H$  normalized by natural period of the material  $t_{mat}$  for different values of impact diameters  $d_H = 10 - 160 \mu\text{m}$  at the same peak impact stress  $\sigma_H = 3 \text{ GPa}$ . Both the axes are on log scale.

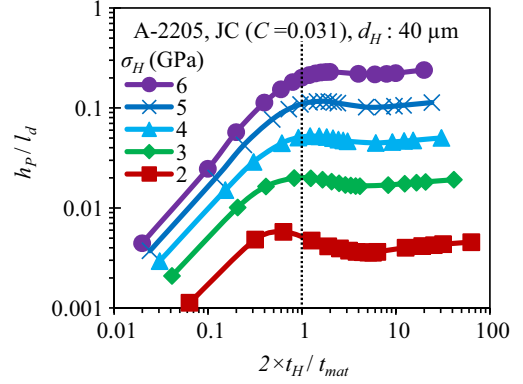


Fig. 13. Variation of pit depth  $h_p$  normalized by plastic strain field size  $l_d$  versus impact duration  $2 \times t_H$  normalized by the natural period of the material  $t_{mat}$  for different values of peak impact stresses  $\sigma_H = 2 - 6 \text{ GPa}$  at the same impact diameter  $d_H = 40 \mu\text{m}$ . Both the axes are on log scale.

of the material. As can be seen, the ratio of  $h_p/l_d$  is also almost independent of  $d_H$  when  $\sigma_H$  is constant.

Unlike Fig. 8, in Fig. 13 also, all the peaks for different values of  $\sigma_H$  at constant value of  $d_H$  are now aligned close to 1 on the horizontal axis as shown by the dotted line, though the deviation is more for  $\sigma_H = 2 \text{ GPa}$ . Unlike Fig. 12, the ratio of  $h_p/l_d$  is not independent of  $\sigma_H$  when  $d_H$  is constant.

Thus based on the above analyses we could state that the dynamics of cavitation pit formation under cavitation hydrodynamic impact is similar to the steady state response of a spring mass damper system under external force. When the impact duration is very short, the frequency of the impact load is very high, hence inertia of the material controls the deformation rather than the stiffness of the material and, most of the energy is converted into kinetic energy leading to very shallow pit depth, as seen in Fig. 5. When the impact duration or frequency is close to the natural time or frequency of the target material the deformation is maximum leading to a maximum pit depth. If the impact duration is higher than the natural time of the material, solution moves towards the static condition and stiffness of the material starts to control the deformation. Depending on the strain rate sensitivity of the material pit depth varies but most of the energy is spent on work-done.

## 5.2. Analysis of cavitation pit dimensions

A simulation campaign of 425 simulations has been conducted for different values of  $\sigma_H$  (2–6 GPa),  $d_H$  (10–160  $\mu\text{m}$ ) and  $t_H$  (0.001–1  $\mu\text{s}$ ) of the Gaussian pressure field and using the strain rate sensitive material properties defined by the JC plasticity model, as in Eq. (1). As an example, Fig. 14 shows the distribution of pit depth  $h_p$  and diameter  $d_p$  for a characteristic impact rise duration  $t_H = 0.05 \mu\text{s}$  and different values of  $\sigma_H$  and  $d_H$ . Point to be noted, pit diameter is always measured at mid-pit depth to be consistent with the experimental measurement of pit diameter to avoid surface noise effect as described in [18]. One interesting fact to be noticed in Fig. 14 is that for a pit of given depth and diameter ( $h_p, d_p$ ) there is only one set of impact load parameters ( $\sigma_H, d_H$ ) that can produce the pit when the impact duration is known. This kind of bijective behavior or one-to-one correspondence between the pit dimensions and the hydrodynamic impact parameters has earlier been reported by Roy et al. [18] within the framework of FEM static analysis of cavitation pitting. This one-to-one correspondence is very essential for estimating hydrodynamic impact loads from pit geometries by the inverse FEM technique as described in [18,20].

Note that in Fig. 14 the impact rise duration is assumed to be the same, irrespective of the impact diameter  $d_H$ , which seems to be a little bit unrealistic from the fluid dynamics point of view. The reason for this assumption is that, although experimental measurements of impact duration due to cavitation bubble collapse are available in the literature, no method is available to derive the impact duration corresponding to a given cavitation pit, at least by the current state of art. Computational fluid dynamics (CFD) simulation of cavitation bubble collapse has been the common practice to correlate collapse duration with bubble size and/or collapse standoff distance [1], but still there is no useable relationship between pit shape and impact duration. In [4] Franc et al. have stated that the impact duration of cavitation bubble collapse is on the order of the ratio of bubble radius ( $r_b$ ) to the speed of sound in the liquid medium ( $c_l$ ). When the microjet resulting from bubble collapse hits the wall, a very high pressure is applied to the material that can be estimated from the classical water hammer formula  $\rho_l c_l v$  where  $v$  is the velocity of the microjet and  $\rho_l$  is the density of the liquid. Outside the jet, a relatively small pressure is applied corresponding to the ambient pressure in the flow. As a result, a pressure discontinuity or shock wave is generated at the boundary of the jet that propagates inwards at the speed of sound in the liquid. During wave propagation, the wall is progressively unloaded until the shock wave reaches the microjet center, which corresponds to complete unloading. The propagation of the wave from the boundary of the jet to its center requires the time ( $r_b/c_l$ ) that can then be considered as the rise time of the impact pressure. Thus, we could estimate the characteristic impact rise duration  $t_H$  based on the impact diameter  $d_H$  using  $2 \times t_H = d_H/(2 \times c_l)$ . This is what is done in Fig. 15.

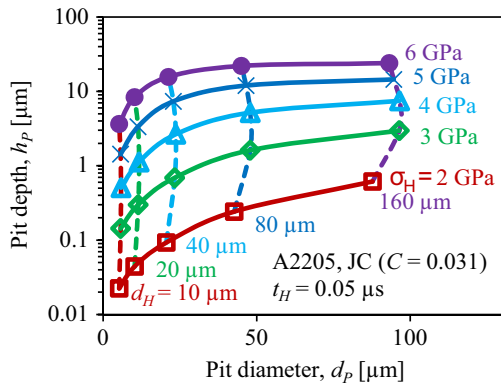


Fig. 14. Distribution of pit depth  $h_p$  and diameter  $d_p$  in A-2205 for a characteristic impact rise duration  $t_H = 0.05 \mu\text{s}$  and different values of  $\sigma_H$  and  $d_H$ . The vertical axis is plotted on log-scale for better readability.

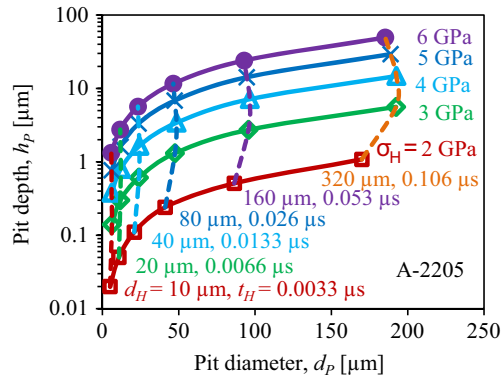


Fig. 15. Distribution of pit depth  $h_p$  and diameter  $d_p$  in A-2205 for different values of  $\sigma_H$  and  $d_H$ . The characteristic impact rise duration  $t_H$  is estimated from  $d_H$ . The vertical axis is plotted on log-scale for better readability.

Unlike Fig. 14 where  $t_H$  was kept constant, in Fig. 15 the characteristic impact rise duration  $t_H$  is estimated from  $d_H$  as stated above. Now also, very interestingly, there exists the one-to-one correspondence between the pit dimensions and the hydrodynamic impact parameters. This opens up a new opportunity for implementing the inverse FEM technique as described in [18,20] for estimating the hydrodynamic impact loads from the cavitation pit geometries by considering the complete dynamic behavior of the target materials. This remains the subject of future research which might give us more accurate estimation of the hydrodynamic impact loads for better quantification of flow aggressiveness. The limitations of such a method would be in selecting a proper material and adequately characterizing its mechanical properties, particularly if the material behavior is size or microstructure dependent. Although the Gaussian pressure field is used for simplicity, the real pressure load applied during bubble collapse is often more complex in both space and time [1]. Knowledge of impact duration corresponding to a given pit, required by the inverse FEM technique for accurate estimation of impact loads, is a big challenge for the time being.

In Fig. 14, it is clear that pit depth  $h_p$  increases with increase in both  $\sigma_H$  and  $d_H$ , whereas pit diameter  $d_p$  increases essentially with increase in  $d_H$ . In Fig. 16, pit shape factor ( $h_p/d_p$ ) is plotted as a function of peak impact stress  $\sigma_H$  (2–6 GPa) on log–log scale for different values of  $d_H$  (10–60  $\mu\text{m}$ ) and  $t_H = 0.01, 0.05$  and  $0.5 \mu\text{s}$ . Different types of points indicate different characteristic impact diameters ( $d_H$ ) and different types of lines, each of which joins the iso- $d_H$  data points, indicate different characteristic impact rise durations ( $t_H$ ). As can be seen, for a given value of  $d_H$  and  $t_H$ , pit shape factor  $h_p/d_p$  follows a power law behavior with  $\sigma_H$ . When  $t_H$  is  $\geq 0.05 \mu\text{s}$  (dotted and dashed lines),  $h_p/d_p$  becomes almost independent of  $d_H$  and  $t_H$  and, follows almost a unique curve (for example dashed lines). This type of unique behavior was studied by Roy et al. [18] with FEM static analysis. The analytical method they proposed to predict peak impact stress from cavitation pit geometry is here extended to complete dynamic behavior of the target material under cavitation pitting.

In Fig. 17 the ratio of pit diameter to impact diameter ( $d_p/d_H$ ) is plotted as a function of the impact diameter  $d_H$  for different values of  $\sigma_H$ , which shows  $d_p/d_H$  remains almost constant irrespective of the value of  $\sigma_H$ , though the error limit increased from  $\pm 5.0\%$  at  $d_H = 10 \mu\text{m}$  to  $\pm 12.0\%$  at  $d_H = 160 \mu\text{m}$ . It should be remembered that unlike  $d_H$ , the pit diameter  $d_p$  is measured at mid-pit depth, hence the ratio  $d_p/d_H$  is close to 0.5. This indicates that actual pit diameter and impact diameter are very close to each other. Earlier by FEM static analysis Roy et al. [18] have seen a similar behavior, which seems to be true if inertial and strain rate sensitivity are

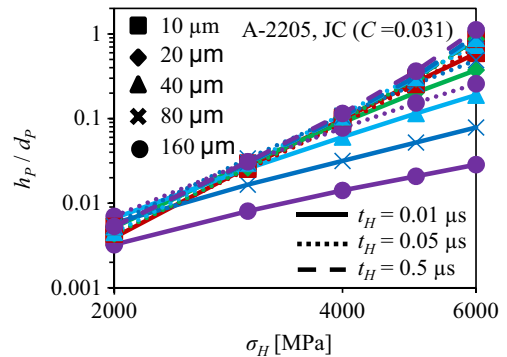


Fig. 16. Pit shape factor ( $h_p/d_p$ ) as a function of peak impact stress  $\sigma_H$  for different values of  $d_H$  (10–60  $\mu\text{m}$ ) and  $t_H = 0.01, 0.05$  and  $0.5 \mu\text{s}$ . Each line joins the iso- $d_H$  data points where different line types indicate different values of  $t_H$  and different point types indicate different  $d_H$ . Linear behavior on log–log graph indicate power law behavior.

included into the simulation. This could be used to predict impact diameter from cavitation pit geometry for a given target material.

### 5.3. Strain rate during cavitation pit formation

Knowledge of strain rate involved in pit formation due to cavitation bubble collapse is important for mass loss prediction [1,2,4] or quantification of flow aggressiveness [19,20,23]. Though there is no solid way to justify, generally strain rate of  $10^3 \text{ s}^{-1}$  or more is used [2,4,23]. With the current state of art, to the best of our knowledge, we cannot measure it experimentally. Numerical approach (FEM) has been adopted here to estimate the maximum strain rate achieved during pitting.

The deformation in cavitation pitting is not homogeneous around a pit (Fig. 9), so that the strain rate would be different at different points into the material. Hence, the determination of maximum strain rate would be a good indicator. For example, as shown in Fig. 18, maximum of maximum principal strain rate ( $\dot{\epsilon}$ ) in A-2205 is plotted as a function of characteristic impact rise duration  $t_H$  for constant values of  $\sigma_H = 3 \text{ GPa}$  and  $d_H = 40 \mu\text{m}$ . In a log-log graph  $\dot{\epsilon}$  versus  $t_H$  follows a linear behavior. This type of behavior was observed in Al-7075 and NAB material as well. Thus we could conclude that for metal, maximum of maximum principal strain rate ( $\dot{\epsilon}$ ) follows a power law behavior with impact rise duration  $t_H$  as given by Eq. (7) (plotted by dotted line in Fig. 18).

$$\dot{\epsilon} = S_3 t_H^{S_4} \quad (7)$$

In Eq. (7),  $S_3$  and  $S_4$  are fitting constants and can be obtained by numerical cavitation pitting analysis of the target material. These

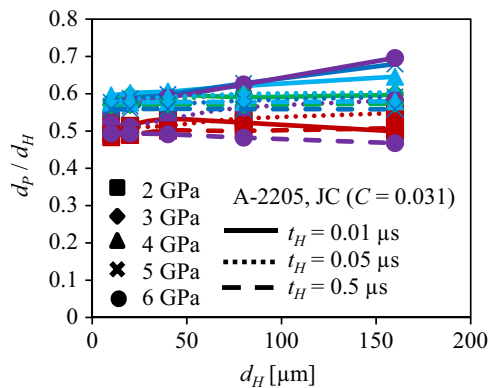


Fig. 17. Ratio of pit diameter to impact diameter ( $d_p/d_H$ ) as a function of impact diameter  $d_H$  for different values of  $\sigma_H$  (2–6 GPa) and  $t_H = 0.01, 0.05$  and  $0.5 \mu\text{s}$ . Each line joins the iso- $\sigma_H$  data points where different line types indicate different values of  $t_H$  and different point types indicate different  $\sigma_H$ .

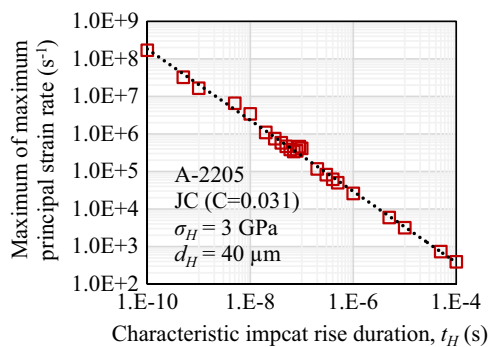


Fig. 18. Plot of maximum of maximum principal strain rate ( $\dot{\epsilon}$ ) versus characteristic impact rise duration  $t_H$  (on log-log scale) for constant values of  $\sigma_H = 3 \text{ GPa}$  and  $d_H = 40 \mu\text{m}$ . Dotted line represents the power law fitting.

two constants would depend on the material properties and impact loading condition (i.e.  $\sigma_H$  and  $d_H$ ).

From Fig. 18, it is clear that strain rate in cavitation pitting depends on the impact duration and may be very high. Now if we consider an impact of size  $d_H = 2 \text{ mm}$  and the speed of sound in water  $c_l \approx 1500 \text{ m/s}$ , then the characteristic impact rise duration  $t_H$  can be estimated as stated in [4] using  $2 \times t_H = d_H / (2 \times c_l)$ . This yields  $t_H \approx 0.333 \mu\text{s}$  for which the strain rate would be  $\sim 10^5 \text{ s}^{-1}$  in A-2205. Probability of such a large impact of 2 mm size would be very rare in cavitation pitting. From our earlier experiences [18–20] on cavitation pitting test, the characteristic mean size of hydrodynamic impacts is close of  $50 \mu\text{m}$ , for which the corresponding impact rise time  $t_H \approx 0.0166 \mu\text{s}$  and strain rate would be  $\sim 10^6 \text{ s}^{-1}$  in A-2205 material. Thus Fig. 18 gives us a more reliable indication of level of strain rate into a metal subjected to cavitation hydrodynamic impact. It should be re-emphasized here that the analytical measurement of  $t_H$  as stated in [4] using  $2 \times t_H = d_H / (2 \times c_l)$  is not universal. It is used here to have a rough idea of the strain rate. Though it is debatable, impact duration in cavitation pitting is assumed to be of the order of microsecond [27], for which the strain rate would be about  $10^5 \text{ s}^{-1}$ .

## 6. Conclusions

Dynamic behavior of cavitation pitting has been analyzed in this paper in details and some interesting phenomena have been observed. It is well established that if the peak stress of the hydrodynamic impact is less than a certain value for which the local stress into the target material is smaller than the yield stress, then no cavitation pit will form. The current study shows that, even if the peak stress is significantly high but the impact duration very short compared to the characteristic time of the material defined on the basis of its natural frequency, no detectable pit will form into the material. This is because of the dynamic behavior of the material under the hydrodynamic impact load at very high frequency. At high frequency, the dynamic behavior is controlled by the inertia of the material as the velocity or acceleration of the deformation is very high. Most of the supplied energy is converted into as kinetic energy and less energy remains available for deformation or work-done. When the impact duration is high, the frequency is less and the deformation is controlled by the stiffness of the material rather than inertia and sufficient amount of the energy is spent on work-done in terms of elastic-plastic deformation.

Inertia and strain rate sensitivity both influence the pit dimensions in cavitation pitting. In metals, at least for the three materials investigated here, the inertial effect on pit dimension becomes insignificant if the impact duration is greater than about one microsecond, while the strain rate effect is inevitable in cavitation pitting since it affects any impact whatever may be its duration up to about  $10^5 \mu\text{s}$ . With increase in strain rate sensitivity the pit becomes shallow, thus the affected volume of the material under hydrodynamic impact gets reduced. Hence the strain rate sensitivity could be considered beneficial since it would reduce the size of deformed region and thereby mass-loss rate due to cavitation erosion.

It is observed that there exists a one-to-one correspondence between the hydrodynamic impact load and the cavitation pit shape. This is a very important conclusion that would enable us to estimate the hydrodynamic impact load from cavitation pit geometry by numerically reproducing the cavitation pit considering the complete dynamics of the material behavior. This remains the subject of future research.

Rate of strain of material deformation during cavitation pitting depends on the hydrodynamic impact duration and accurate estimation of impact duration either by experimental or numerical

method remains a big challenge for the researchers. Current study shows that, in metals the strain rate could vary in the range of  $10^4$ – $10^7$  s<sup>-1</sup> when the loading time varies between 1 μs and 0.001 μs.

## Acknowledgments

This research was conducted under the Naval International Cooperative Opportunities in Science and Technology Program (NICOP, Grant No. N62909-12-1-7112) funded by the Office of Naval Research. The authors wish to thank Dr. Ki-Han Kim from the Office of Naval Research (ONR) and Dr. Woei-Min Lin from the Office of Naval Research Global (ONRG) who supported this work.

## References

- [1] G.L. Chahine, Modeling of cavitation dynamics and interaction with material, in: K.H. Kim, G.L. Chahine, J.-P. Franc, A. Karimi (Eds.), *Advanced Experimental and Numerical Techniques for Cavitation Erosion Prediction*. Fluid Mechanics and its Applications, 160, Springer, Dordrecht, 2014, pp. 123–162, Chapter 6.
- [2] A. Karimi, J.-P. Franc, Modeling of material response, in: K.-H. Kim, G. L. Chahine, J.-P. Franc, A. Karimi (Eds.), *Advanced Experimental and Numerical Techniques for Cavitation Erosion Prediction*. Fluid Mechanics and its Applications, 160, Springer, Dordrecht, 2014, pp. 163–181, Chapter 7.
- [3] C.-T. Hsiao, A. Jayaprakash, A. Kapahi, J.-K. Choi, G.L. Chahine, Modelling of material pitting from cavitation bubble collapse, *J. Fluid Mech.* 755 (2014) 142–175.
- [4] Fluid mechanics and its applications, in: J.-P. Franc, J.-M. Michel (Eds.), *Fundamentals of Cavitation*, 76, Kluwer Academic Publishers, Dordrecht, 2004.
- [5] N. Berchiche, J.-P. Franc, J.M. Michel, A cavitation erosion model for ductile materials, *J. Fluids Eng.* 124 (2002) 601–606.
- [6] R.T. Knapp, Recent Investigations of the mechanics of cavitation and cavitation damage, *Trans. ASME* 77 (1955) 1045–1054.
- [7] R.T. Knapp, Accelerated field tests of cavitation intensity, *Trans. ASME* 80 (1958) 91–102.
- [8] J.-K. Choi, A. Jayaprakash, G.L. Chahine, Scaling of cavitation erosion progression with cavitation intensity and cavitation source, *Wear* 278–279 (2012) 53–61.
- [9] A. Jayaprakash, J.-K. Choi, G.L. Chahine, F. Martin, M. Donnelly, J.-P. Franc, A. Karimi, Scaling study of cavitation pitting from cavitating jets and ultrasonic horns, *Wear* 296 (1–2) (2012) 619–629.
- [10] H. Soyama, M. Futakawa, K. Homma, Estimation of pitting damage induced by cavitation impacts, *J. Nucl. Mater.* 343 (1–3) (2005) 116–122.
- [11] H. Soyama, High-speed observation of a cavitating jet in air, *J. Fluids Eng.* 127 (6) (2005) 1095–1101.
- [12] H. Soyama, K. Nishizawa, M. Mikami, Enhancement of cavitation aggressivity around a cavitating jet by injecting low-speed water jet for cavitation peening, In: *Proceedings of the 7th International Symposium on Cavitation*, Ann Arbor, Michigan, USA, 2009.
- [13] T. Keil, P.F. Pelz, J. Kadavelil, J. Necker, W. Moser, D. Christ, Droplet impact vs. cavitation erosion, In: *WIMRC 3rd International Cavitation Forum*, University of Warwick, UK, 2011.
- [14] A. Krella, An experimental parameter of cavitation erosion resistance for TiN coatings, *Wear* 270 (3–4) (2011) 252–257.
- [15] J.-P. Franc, Incubation time and cavitation erosion rate of work-hardening materials, *J. Fluids Eng.* 131 (2) (2009) 021303-1–021303-14.
- [16] M. Fivel, J.-P. Franc, S.C. Roy, Towards numerical prediction of cavitation erosion, *Interface Focus* 5 (2015) 20150013-1–20150013-10.
- [17] G.L. Chahine, J.-P. Franc, A. Karimi, Cavitation Impulsive Pressures, in: K.-H. Kim, G.L. Chahine, J.-P. Franc, A. Karimi (Eds.), *Advanced Experimental and Numerical Techniques for Cavitation Erosion Prediction*. Fluid Mechanics and its Applications, 160, Springer, Dordrecht, 2014, pp. 71–95, Chapter 4.
- [18] S.C. Roy, J.-P. Franc, C. Pellone and M. Fivel, Determination of cavitation load spectra – Part 1: Static finite element approach, *Wear*, 2015, accepted for publication.
- [19] S. C. Roy, M. Fivel, J.-P. Franc, C. Pellone, Cavitation induced damage: FEM inverse modeling of the flow aggressiveness, In: *Proceedings of 11th International Conference on Flow Dynamics*, Sendai, Japan, Oct. 2014.
- [20] S.C. Roy, J.-P. Franc, M. Fivel, Cavitation erosion: using the target material as a pressure sensor, *J. Appl. Phys.*, 2015, accepted for publication.
- [21] F. Pöhl, S. Mottyll, R. Skoda, S. Huth, Evaluation of cavitation-induced pressure loads applied to material surfaces by finite-element-assisted pit analysis and numerical investigation of the elasto-plastic deformation of metallic materials, *Wear* 330–331 (618–628) (2015) 1–11.
- [22] G.R. Johnson, W.H. Cook, Fracture characteristics of three metals subjected to various strains, strain rates, temperatures and pressures, *Eng. Fract. Mech.* 21 (1) (1985) 31–48.
- [23] D. Carnelli, A. Karimi, J.P. Franc, Evaluation of the hydrodynamic pressure of cavitation impacts from stress–strain analysis and geometry of individual pits, *Wear* 289 (0) (2012) 104–111.
- [24] J.K. Choi, A. Jayaprakash, A. Kapahi, C.T. Hsiao, G.L. Chahine, Relationship between space and time characteristics of cavitation impact pressures and resulting pits in materials, *J. Mater. Sci.* 49 (8) (2014) 3034–3051.
- [25] J.-P. Franc, M. Riondet, A. Karimi, G.L. Chahine, Material and velocity effects on cavitation erosion pitting, *Wear* 274–275 (0) (2012) 248–259.
- [26] A.P. French, *Vibrations and Waves*, W.W. Norton and Company Inc., New York, 1971.
- [27] *ASM Handbook, Failure Analysis and Prevention*, 11, ASM International, Ohio, USA, 2002.